Dynamic Structure Factors from Lipid Membrane Molecular Dynamics Simulations

Erik G. Brandt and Olle Edholm*
Theoretical Biological Physics, Department of Theoretical Physics, Royal Institute of Technology (KTH), AlbaNova University Center, Stockholm, Sweden

ABSTRACT Dynamic structure factors for a lipid bilayer have been calculated from molecular dynamics simulations. From trajectories of a system containing 1024 lipids we obtain wave vectors down to 0.34 nm^{-1}, which enables us to directly resolve the Rayleigh and Brillouin lines of the spectrum. The results confirm the validity of a model based on generalized hydrodynamics, but also improves the line widths and the position of the Brillouin lines. The improved resolution shows that the Rayleigh line is narrower than in earlier studies, which corresponds to a smaller thermal diffusivity. From a detailed analysis of the power spectrum, we can, in fact, distinguish two dispersive contributions to the elastic scattering. These translate to two exponential relaxation processes in separate time domains. Further, by including a first correction to the wave-vector-dependent position of the Brillouin lines, the results agree favorably to generalized hydrodynamics even up to intermediate wave vectors, and also yields a 20% higher adiabatic sound velocity. The width of the Brillouin lines shows a linear, not quadratic, dependence to low wave vectors.

INTRODUCTION

The dynamics of biological membranes can be characterized and measured in different ways. Some experimental techniques measure the motion of individual atoms and molecules, whereas others probe more or less collective motions. Molecular dynamics (MD) simulations produce trajectories of the individual atomic motions, but may also be analyzed in terms of collective motions. Here we concentrate on the application of such simulations to reproduce and interpret collective motions. Inelastic scattering of x rays or neutrons (1–3) traditionally probes local density fluctuations at short time- and length-scales, typically 10^{-12} s and 10^{-10} m. Advances in neutron scattering techniques based on spin-echoes have recently extended these scales dramatically (4). On longer time- and length-scales, (Brillouin) light scattering can be used to probe the hydrodynamic behavior. This has been done for simple liquids (5). The theoretical framework wherein all these experiments are interpreted is generalized hydrodynamics (6,7). At an early stage, MD simulations were employed as a complement to experiments for monitoring this kind of dynamics (8–13). Data obtained from simulations of a few hundred simple liquid atoms for some hundreds of picoseconds, showed features predicted by generalized hydrodynamics, in agreement with the experiments (5,14,15). Taken all together, this furnished strong evidence for the validity of generalized hydrodynamics for simple liquids.

Lipid bilayers are fluidlike in two (lateral) dimensions, but they are ordered in the third (normal) dimension. The hydrocarbon core consists of fatty acid chains that are dominated by the nonbonded Lennard-Jones interactions. This means that motions in the lateral dimensions have similarities with simple Lennard-Jones fluids like Argon. The connectivity of the chains in the normal dimension, and the electrostatic interactions in the headgroup/water region makes, however, the lateral motion over larger distances slower, different, and more complex, compared to that in simple fluids. Biological membranes show dynamics on many temporal and spatial scales (see, e.g., (16)). This includes coherent collective motions like undulations of the bilayer, area-thickness fluctuations, and more localized motions involving fewer atoms, like the reorientation of the hydrocarbon tails of the lipids (which has been extensively monitored by nuclear magnetic resonance techniques).

Traditional experimental inelastic scattering from membranes covers angular frequencies in the interval $(0.4–40) \times 10^{12}$ rad/s ($E = \hbar\omega = 0.25$–25 meV), and wave vectors in the approximate interval 4.5–30 nm^{-1} (1,2). Advances in neutron scattering using spin-echo techniques (4,17) have extended this wave vector interval with several orders of magnitude down to 0.01 nm^{-1}. The rapid angular frequencies corresponding to timescales in the picosecond range are easily accessible in MD simulations, even though experiments as well as simulations require a substantial amount of sampling to produce something beyond noise.

The high wave vectors, which translate to short wavelengths, can, without trouble, be reached from MD simulations. When the wave vectors become much larger than the inverse distance between nearest-neighbor lipids, the continuum picture will eventually break down. The details of how and when this occurs is an interesting problem in itself but not the focus of this study. Instead, we concentrate on the other end of the wave vector interval, where we expect continuum theories like generalized hydrodynamics to be valid. Earlier simulation studies on pure lipid bilayers have restricted their studies to vectors down to ~4.5 nm^{-1}. It is

Submitted July 1, 2008, and accepted for publication November 17, 2008.

*Correspondence: oed@kth.se

Editor: Peter Tieleman.

0006-3495/09/03/1828/11 $2.00

doi: 10.1016/j.bpj.2008.11.044

clear from experiments (18) as well as those simulations (19) that one is just starting to probe the hydrodynamic regime at these distances. It is thus highly desirable to extend the monitored wave vectors further down in experiments as well as simulations. In the latter case, this is solely a question of simulating a large enough system for long enough time. The aim here is to push the length-scale one order of magnitude and run the system long enough to get reliable statistics that makes a direct comparison with theory possible without using window functions or running averages. The hope is also to determine macroscopic material constants from a microscopic description in agreement with a continuum picture. For this purpose, we have studied a system consisting of 1024 lipids in six separate 24-ns simulations and are able to probe the dynamic structure factor down to 0.34 nm^{-1}. One may note that this corresponds to a 16-times-larger system simulated for orders-of-magnitude longer time than the pioneering study by Tarek et al. (19).

The results show that, for low wave vectors, the lipid bilayer can be described by the linearized hydrodynamic equations, which lead to the well-known Rayleigh-Brillouin triplet shape of the dynamic structure factor. However, as the wave vectors increase, the deviations appear, as described in Results and Discussion. Material constants were extracted from the low wave vectors and were found in agreement with known results.

THEORY

The atomistic picture: density-density correlation functions

Equilibrium fluctuations in the local number density $\rho(\mathbf{r}, t)$ of a liquid may be characterized by the van Hove correlation function (20)

$$G(\mathbf{r},t) = \frac{V}{N}\langle\rho(\mathbf{r}_0,t_0)\rho(\mathbf{r}_0 + \mathbf{r}, t_0 + t)\rangle. \quad (1)$$

Here V is the volume, N the number of particles, and the brackets denote an average over all initial times t_0 and positions $\mathbf{r}_0$. For a system consisting of N pointlike particles the number density can be expressed as

$$\rho(\mathbf{r},t) = \sum_{l=1}^{N}\delta(\mathbf{r} - \mathbf{r}_l(t)), \quad (2)$$

which means that the van Hove correlation function may be written

$$\begin{aligned} G(\mathbf{r},t) &= \tfrac{V}{N}\sum_{l,m}\big\langle\delta(\mathbf{r}_0 - \mathbf{r}_l(t_0))\,\delta(\mathbf{r}_0 + \mathbf{r} - \mathbf{r}_m(t + t_0))\big\rangle \\ &\equiv \frac{1}{N}\frac{1}{T}\sum_{l=1}^{N}\sum_{m=1}^{N}\int_0^T dt_0\int_{\mathbb{R}^3} d^3\mathbf{r}_0\,\delta(\mathbf{r}_0 - \mathbf{r}_l(t_0)) \\ &\quad\times\delta(\mathbf{r}_0 + \mathbf{r} - \mathbf{r}_m(t + t_0)), \end{aligned} \quad (3)$$

where the time average over a finite time interval of length T has been explicitly written as an integral. Because the lipid bilayer is fluidlike only in the lateral dimensions (x, y), we average over the normal direction (z) and, from now on, regard only correlation functions in two dimensions. We then introduce a spatial Fourier representation of the number density

$$\widehat{\rho}(\mathbf{k},t) = \int_{\mathbb{R}^2} d^2\mathbf{r}\;\; e^{i\mathbf{k}\cdot\mathbf{r}}\;\;\rho(\mathbf{r},t) = \sum_{l=1}^{N} e^{i\mathbf{k}\cdot\mathbf{r}_l(t)}. \quad (4)$$

The system is isotropic in x and y and thus $\rho(\mathbf{k}, t)$ will not depend on the direction of $\mathbf{k}$ but upon $|\mathbf{k}| \equiv k$ only. Following the procedure of Boon and Yip (6), the intermediate scattering function is introduced as the spatial Fourier transform of the van Hove correlation function

$$\begin{aligned} F(k,t) &= \int_{\mathbb{R}^2} d^2\mathbf{r}\, e^{i\mathbf{k}\cdot\mathbf{r}}\, G(\mathbf{r},t) \\ &= \frac{1}{T}\int_0^T dt_0\,\widehat{\rho}^*(k,t_0)\widehat{\rho}(k,t_0 + t), \end{aligned} \quad (5)$$

with the asterisk denoting complex conjugation. The dynamic structure factor, $S(k, \omega)$, which is directly determined in scattering experiments, is the temporal Fourier transform of the intermediate scattering function

$$\begin{aligned} S(k,\omega) &= \int_{-\infty}^{\infty} dt\, e^{-i\omega t}F(k,t) = \widehat{\widehat{\rho}}^*(k,-\omega)\widehat{\widehat{\rho}}(k,\omega) \\ &= \left|\widehat{\widehat{\rho}}(k,\omega)\right|^2, \end{aligned} \quad (6)$$

with the Fourier transform in time and space of the number density being

$$\widehat{\widehat{\rho}}(k,\omega) = \sum_{l=1}^{N}\int_{-\infty}^{+\infty} dt\, e^{i(\mathbf{k}\cdot\mathbf{r}_l(t) - \omega t)}. \quad (7)$$

We note that since $F(k, t)$ is a real function which is even in t, the dynamic structure factor will be even in ω. The numerical computation of $S(k, \omega)$ is considerably simplified since the time integral in Eq. 5 is a convolution integral, which will generate a simple square in Fourier space.

Another quantity of interest is the longitudinal current, defined as

$$\mathbf{j}(\mathbf{r},t) = \sum_{l=1}^{N}\frac{d\mathbf{r}_l(t)}{dt}\,\delta(\mathbf{r} - \mathbf{r}_l(t)). \quad (8)$$

It is easily shown (see, e.g., (6)) that the Fourier transform in time and space of the correlation function of this current is directly given in terms of the dynamic structure factor from the relation

$$J(k,\omega) = \frac{\omega^2}{k^2}S(k,\omega). \quad (9)$$

Depending on the situation, it may be convenient to study one or the other of these quantities.

The continuum picture: generalized hydrodynamics

The hydrodynamic equations are phenomenological transport equations, valid at temporal and spatial scales for which the properties of the liquid vary weakly. We give here a brief review of the derivation of $S(k, \omega)$ from these equations. More detailed treatments may be found in the literature (6,7,21).

The state of the liquid is characterized by the number density $\rho(\mathbf{r}, t)$, the absolute temperature $T(\mathbf{r}, t)$, and the velocity $\mathbf{v}(\mathbf{r}, t)$. The treatment is simplified by separating out the uniform equilibrium number density ρ_0 and temperature T_0, leaving us with the fluctuating variables $\rho_1(\mathbf{r}, t) = \rho(\mathbf{r}, t) - \rho_0$ and $T_1(\mathbf{r}, t) = T(\mathbf{r}, t) - T_0$, which obey three equations. These are the continuity equation which accounts for the conservation of the particle number, the linearized Navier-Stokes equation, which accounts for the conservation of momentum and the energy transport equation,

$$\left.\begin{aligned} \tfrac{\partial \rho_1}{\partial t} + \rho_0 \nabla \cdot \mathbf{v} &= 0 \\ \rho_0 \frac{\partial \mathbf{v}}{\partial t} + \frac{c^2}{\gamma}[\nabla \rho_1 + \alpha \rho_0 \nabla T_1] - \left(\frac{4}{3}\eta_S + \eta_B\right)\nabla(\nabla \cdot \mathbf{v}) &= 0 \\ \rho_0 c_V \frac{\partial T_1}{\partial t} - \frac{c_V(\gamma - 1)}{\alpha}\frac{\partial \rho_1}{\partial t} - \lambda \nabla^2 T_1 &= 0 \end{aligned}\right\}. \tag{10}$$

In these expressions, c is the adiabatic sound velocity, and $\gamma = c_P/c_V$ is the ratio between the specific heats at constant pressure, c_P, and constant volume, c_V. Further, the equations contain the shear and bulk viscosities η_S and η_B, the thermal expansion coefficient α, and the thermal conductivity λ. The equations describe the fluid as a locally homogeneous and isotropic continuum at (local) thermodynamic equilibrium for which the transport processes are described by linear laws with constant coefficients.

Elimination of the velocity and introduction of Fourier-Laplace representations for the density and temperature leads to a closed analytical expression for the Fourier-Laplace transform of the number density

$$\begin{aligned} \tilde{\hat{\rho}}(k, s) &= \int_0^\infty \mathrm{d}t\, e^{-st} \int_{\mathbb{R}^2} \mathrm{d}^2\mathbf{r}\, e^{i\mathbf{k}\cdot\mathbf{r}}\, \rho_1(\mathbf{r}, t) \\ &= \hat{\rho}(k) \frac{s^2 + (a + b)k^2 s + abk^4 + c^2(1 - \gamma^{-1})k^2}{s^3 + (a + b)k^2 s^2 + \left(c^2k^2 + abk^4\right)s + \gamma^{-1}c^2 a k^4}, \end{aligned} \tag{11}$$

where $a = {\rho_0}^{-1}{c_V}^{-1}\lambda$ and $b = \rho_0^{-1}(\frac{4}{3}\eta_S + \eta_B)$. The denominator is a third-order dispersion equation with the roots given in a small k-expansion as

$$\begin{aligned} s_0 &= -\gamma^{-1}ak^2 + \mathrm{O}\left(k^4\right), \\ s_\pm &= \pm i\left(ck + \mathrm{O}\left(k^3\right)\right) - \tfrac{1}{2}(a(1 - \gamma^{-1}) + b)k^2 + \mathrm{O}\left(k^4\right). \end{aligned} \tag{12}$$

Exact expressions for the three roots are formally available but not very practical due to their complexity. The higher order terms of Eq. 12 have anyhow been worked out in detail elsewhere (22).

Using Eq. 11 we may construct the Laplace-Fourier transformed density-density correlation function $\langle \hat{\rho}^*(k)\tilde{\hat{\rho}}(k, s)\rangle$, and from this the dynamic structure factor

$$S(k, \omega) = 2\,\mathrm{Re}\lim_{\epsilon \to 0}\left\langle \hat{\rho}^*(k)\tilde{\hat{\rho}}(k, s = \epsilon + i\omega)\right\rangle. \tag{13}$$

The last relation holds because $S(k, \omega)$ is real and an even function of ω. We identify the static structure factor as

$$S(k) = \frac{1}{2\pi}\int_{-\infty}^{+\infty} \mathrm{d}\omega\, S(k, \omega) = \left\langle \hat{\rho}^*(k)\hat{\rho}(k)\right\rangle, \tag{14}$$

and make a somewhat tedious partial fraction of Eq. 11. Some additional algebraic manipulations finally yield

$$\begin{aligned} \frac{S(k, \omega)}{S(k)} = A_0 \frac{\Gamma_h}{\omega^2 + \Gamma_h^2} + A_s \Bigg[&\frac{\Gamma_s + \xi(\omega + \omega_s)}{(\omega + \omega_s)^2 + \Gamma_s^2} \\ &+ \frac{\Gamma_s - \xi(\omega - \omega_s)}{(\omega - \omega_s)^2 + \Gamma_s^2}\Bigg]. \end{aligned} \tag{15}$$

To obtain this functional form for $S(k, \omega)$ the notation has been simplified by introducing a number of parameters. With $S(k)$ defined as in Eq. 14, these are $A_0 = 2(\gamma - 1)/\gamma$; $A_s = 1/\gamma$; $\Gamma_h(k) = D_T k^2$; $\Gamma_s(k) = \beta k^2$; and $\omega_s(k) = ck$, where $D_T = \gamma^{-1}a$ is the thermal diffusivity. The sound attenuation coefficient β is $\frac{1}{2}(a(1 - \gamma^{-1}) + b)$ and the asymmetry parameter is given by $\xi(k) = [\beta + D_T(\gamma - 1)]c^{-1}k$. A schematic plot of Eq. 15 versus ω is shown in Fig. 1.

Hence the power spectrum becomes a Rayleigh-Brillouin triplet consisting of three Lorentzian lines with widths Γ_h and Γ_s centered at $\omega = 0$ and $\omega = \pm\omega_s$, with $\xi(k)$ determining the asymmetry of the two Brillouin lines and causing a slight shift of these toward the central Rayleigh peak.

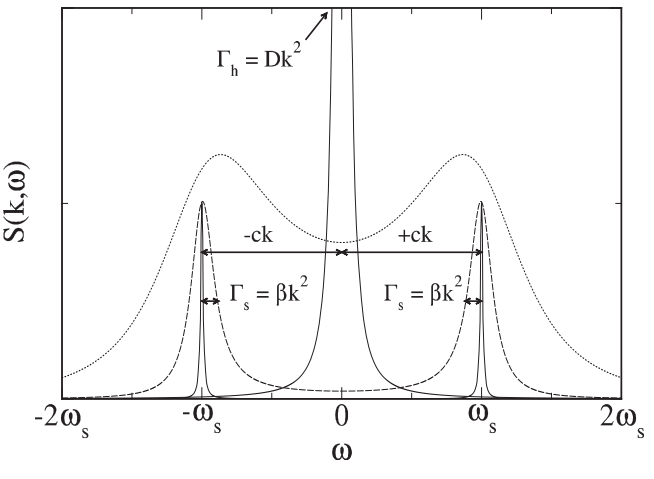

FIGURE 1 Schematic view of the dynamic structure factor according to a three-mode model. Typical Rayleigh and Brillouin peaks are drawn with solid lines and also Brillouin lines for larger values of k where the asymmetry appears (*dashed* and *dotted lines*).

METHODS

Simulations setup

Molecular dynamics (MD) simulations were performed with the GROMACS 3.3.2 software (23), on a patch of dimyristoyl phosphatidylcholine (DMPC) membrane bilayer consisting of 1024 lipids, 512 in each leaflet. The simulation box used for production runs was a rectangular parallelepiped of size 18.55 × 16.55 × 5.82 nm with periodic boundary conditions employed in all directions. The force field used was that of Berger et al. (24), which provides a united-atom model for the hydrocarbon groups of the lipid molecules. Lennard-Jones interactions were treated with a 1.0-nm cutoff and the long-range electrostatic interactions using PME (25,26) beyond 1.0 nm, the same radius as for the neighbor list (which was updated every 10th simulation step). The equations of motion were integrated with a Verlet algorithm using a 4-fs time step and constraints on bond lengths.

The system was prepared from a smaller, well-equilibrated configuration consisting of 256 fully hydrated DMPC molecules ($n_w = 23$ water molecules per lipid), which was replicated four times and put together into one large patch. The large system was then equilibrated for 10 ns in the isothermal-isobaric (NPT) ensemble, controlling the temperature at 300 K and the pressure at 1 bar, using the Berendsen weak coupling algorithms (27). After that the Nosé-Hoover thermostat (28,29) and the Parrinello-Rahman barostat (30,31) were used to ensure correct ensemble dynamics, resulting in a stable L_α-phase of the lipids with an area per lipid $A_L = 0.60\ \mathrm{nm}^{-2}$, in agreement with experimental data (32,33). The lateral box dimensions and A_L were kept fixed in the final simulations by setting the compressibilities in the x and y directions to zero. The pressure in the z direction was fixed to 1 bar using the Parrinello-Rahman barostat. This anisotropic coupling resulted in a negligible surface tension and kept the reciprocal k-vectors fixed throughout the simulations.

Six identical systems were set up and simulated with separate initial atomic velocities (generated as Maxwell-Boltzmann distributions from different random seeds), allowing statistics to be collected from independent simulations. Each system was simulated continuously for 24 ns. In theory, this allows the sampling of correlation functions in the time domain from 4 fs up to 24 ns (corresponding to energy transfers from 1 eV down to 0.17 μ eV). In practice, the decay of the correlation function and poor statistics especially at long times and for small wave vectors result in statistical errors of similar size to the correlation function itself beyond 0.4–4 ns. For the main part of the analysis, we have therefore restricted us to the time interval up to 400 ps corresponding to 0.01 meV. In an effort to resolve the Rayleigh line in more detail at small angular frequencies, we extended this analysis to 4 ns (0.001 meV).

Correlation functions from MD trajectories

$S(k, \omega)$ was calculated as the absolute square of the time and space Fourier transform of the atom number density (Eq. 7). Since the scattering in lipid bilayers is dominated by the hydrocarbon groups (34) (unless some special experimental technique or selective deuteration is used), the analysis was restricted to the hydrocarbon groups of the lipid tails. The correlation functions were calculated from the position of the bead representing the united atom CH_2 groups. Further, we averaged over the z coordinates and over circles with radii $k = \sqrt{k_{n_i}^2 + k_{n_i}^2}$, where $i = \{x, y\}$. The periodic boundary conditions in the simulations restrict the components of the wave vectors to $k_{n_i} = \frac{2\pi}{L_i} n_i$, where n_i values are positive integers and L_i the simulation box length in the i direction. All reciprocal wave vectors were sorted into equally spaced bins in k space. The restrictions on the reciprocal vectors in combination with the box size rendered a resolution of $2\pi/L_{max} \approx 0.34\ \mathrm{nm}^{-1}$ in k space. Starting at this value, we analyzed wave vectors up to 30 nm^{-1}, above which real space distances are too small (< 0.2 nm) for collective dynamics to be relevant.

Continuous chunks of full-precision MD trajectories were used for the calculation of the dynamic structure factors. The angular frequency resolution $\Delta\omega = 2\pi/T$ is limited by the simulation length T. For all calculations and analysis, $T = 400$ ps (corresponding to $\Delta\omega = 0.01$ meV) was used. In addition, when determining the width of the Rayleigh line, an improved resolution of $\Delta\omega = 0.001$ meV was tested using $T = 4$ ns. Data was saved densely (every time-step $\Delta t = 4$ fs) in the simulations so that 20 sampled points in each Fourier period produced accurate angular frequencies up to $2\pi/(20\Delta t) \approx 50$ meV.

The procedure for computing the dynamic structure factor was to first construct the Fourier representation of the atom number density, $\widehat{\rho}(k,t)$, as a (complex) sum of exponentials (Eq. 4) directly from the full-precision MD trajectory. That was done for each time step in all chunks. After completion of $\widehat{\rho}(k,t)$ for a chunk, the huge trajectory was deleted to save space. Storing the full MD trajectories would have required ~60 TB storage capacity in total. By operating on the smaller pieces, only ~0.5 TB of data repository was needed.

When $\widehat{\rho}(k,t)$ had been computed for all times, a fast Fourier transform (FFT) algorithm (35) was used for the time transform to calculate $\widehat{\widehat{\rho}}(k,\omega)$, from which the dynamic structure factor is obtained as $S(k,\omega) = |\widehat{\widehat{\rho}}(k,\omega)|^2$. The dynamic structure factors were computed independently for all pieces and all systems and then averaged over all chunks to reduce statistical errors.

The dynamic structure factors computed from the simulation data were numerically fitted to a three-mode model according to Eq. 15 using a Levenberg-Marquardt algorithm (36,37) and normalized with $S(k)$, which was obtained by numerical integration.

The window function

Experimental techniques such as inelastic scattering using x rays (1) or neutrons (2) are limited by the instrumental resolution. Theoretically this corresponds to a convolution of the raw data with a window function. The functional form of the window function depends on the spectrometer, but a Gaussian shape is often a good approximation. However, Lorentzian window functions are often used in the analysis since they preserve the shape of a spectrum consisting of Lorentzians and make an analytical deconvolution of the power spectrum possible. Deviations from that type of shape result in a difference between the convoluted power spectrum and the true power spectrum. To give a more detailed picture of how the power spectrum is influenced by the convolution with a window function of width σ, we applied the Lorentzian

$$\widehat{f}_w(\omega) = \frac{2\sigma}{\omega^2 + \sigma^2}, \tag{16}$$

to our raw $S(k, \omega)$ data. Computationally a convolution requires N^2 operations, where in our case $N = 10^5$–10^6. But in the time domain this corresponds to a multiplication of the intermediate scattering function, $F(k, t)$, to an exponential function,

$$f_w(t) = e^{-t/\tau}, \tag{17}$$

with the falloff time τ. Using a FFT algorithm (see above and (35)) the frequency-to-time Fourier transform only requires N operations. Hence, we first perform a backward (inverse) transform of our computed $S(k, \omega)$ to get $F(k, t)$. We then multiply with the exponential function and carry out a forward transform to get back to $S(k, \omega)$, now convoluted with a Lorentzian window function of width σ (corresponding to the falloff time τ). This procedure was used for three values: $\tau = 2$, 20, and 200 ps. The smallest value is the same as used by Tarek et al. (19).

RESULTS

In this section we give a general overview, followed by a detailed presentation of the results for the Rayleigh and Brillouin lines. Finally the Landau-Placzek ratio is

calculated. We focus on the regime of small wave vectors, i.e., the behavior in the hydrodynamic limit. The comparison to a three-mode model was done by fitting the data to Eq. 15 as a function of ω for fixed values of k.

Most important is that the quality of the data permits a high-energy resolution ($\Delta\omega = 0.01$ meV) of $S(k, \omega)$ for reciprocal k values in the interval 0.34–30 nm^{-1}. The spectrum can be divided into three distinct domains: Low, $k < 5$ nm^{-1} (wavelengths $\lambda > 1.2$ nm); intermediate, $5 < k < 20$ nm^{-1} ($1.2 > \lambda > 0.3$ nm); and high, $k > 20$ nm^{-1} ($\lambda < 0.3$ nm). Fig. 2 shows the dynamic structure factor for a number of selected wave vectors in all domains. In Fig. 3 , we illustrate how different amounts of sampling affect the dynamic structure factor at the lowest wave vectors.

In the low k regime the dynamic structure factor is well described by a Rayleigh-Brillouin triplet as predicted by generalized hydrodynamic theory. For intermediate wave vectors, the spectrum can still be described by three Lorentzians but the predicted relations from hydrodynamic theory are no longer fulfilled. The Brillouin peaks more and more take the shapes of shoulders on the Rayleigh peak, while, at still larger wave vectors, the spectrum tends to three Lorentzians at $\omega = 0$, making a separation of the Rayleigh line and the Brillouin doublet unworkable. This trend is characterized by a dispersion gap for the propagation of acoustic waves and de Gennes narrowing of the power spectrum (38). In the high domain (k up to 30 nm^{-1}), the spectrum is dominated by the diffusive Rayleigh line, whereas the intensities of the Brillouin lines are low. The Rayleigh line showed distinct deviations from Lorentzian functional form in this regime.

The material constants from the hydrodynamic equations that appear in the equation for $S(k, \omega)$ (Eq. 15) were extracted from the low k domain data (Table 1). These were the thermal diffusivity D_T, the sound-attenuation coefficient β, the sound velocity c, and the ratio of the specific heats γ. They were all determined, in fair agreement with known experimental values (39–42). Compared to some of the earlier studies of collective chain dynamics in lipid bilayers

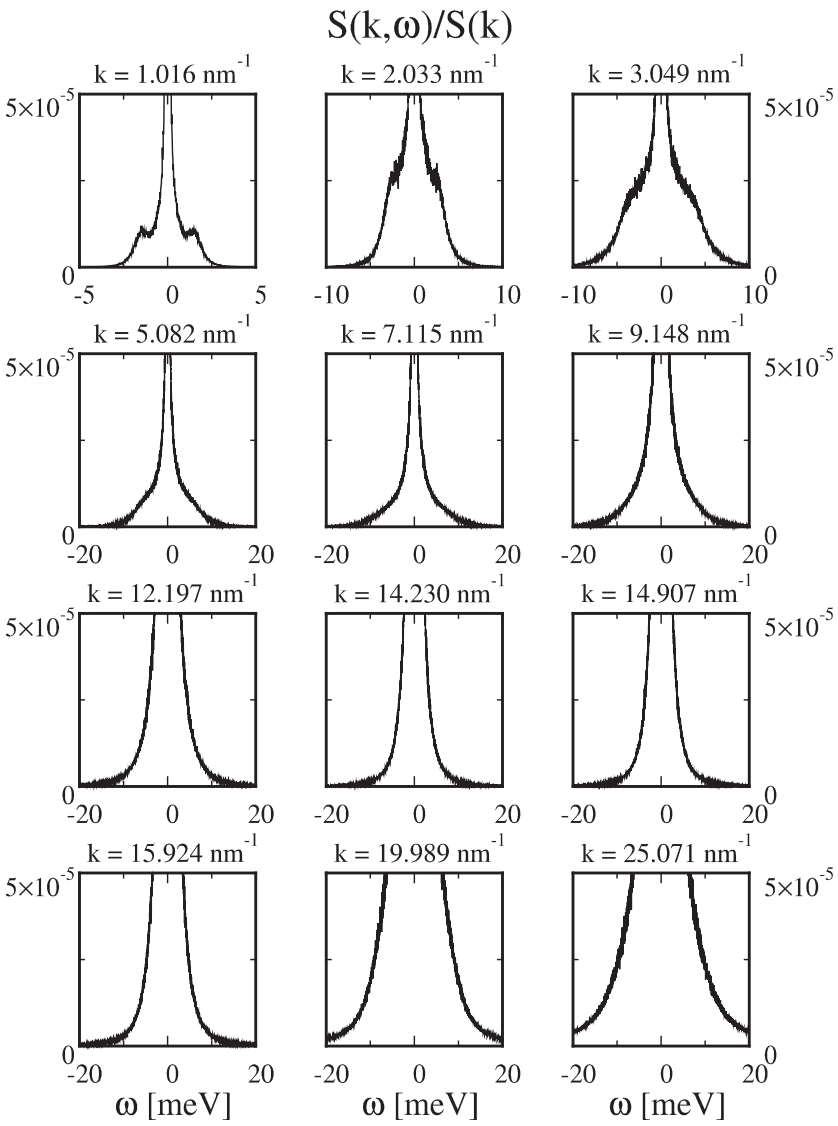

FIGURE 2 Dynamic structure factors for selected wave vectors. In the low domain, $k < 5$ nm^{-1}, the spectrum is a Rayleigh-Brillouin triplet. The intermediate regime, $5 < k < 20$ nm^{-1}, shows the Brillouin modes as shoulders on the Rayleigh line, which eventually center and lead to a dispersion gap (de Gennes narrowing) in the bilayer at ~k_G. In the high domain, $k >$ 20 nm^{-1}, the intensities of the Brillouin modes are low and the spectrum is dominated by the thermal mode.

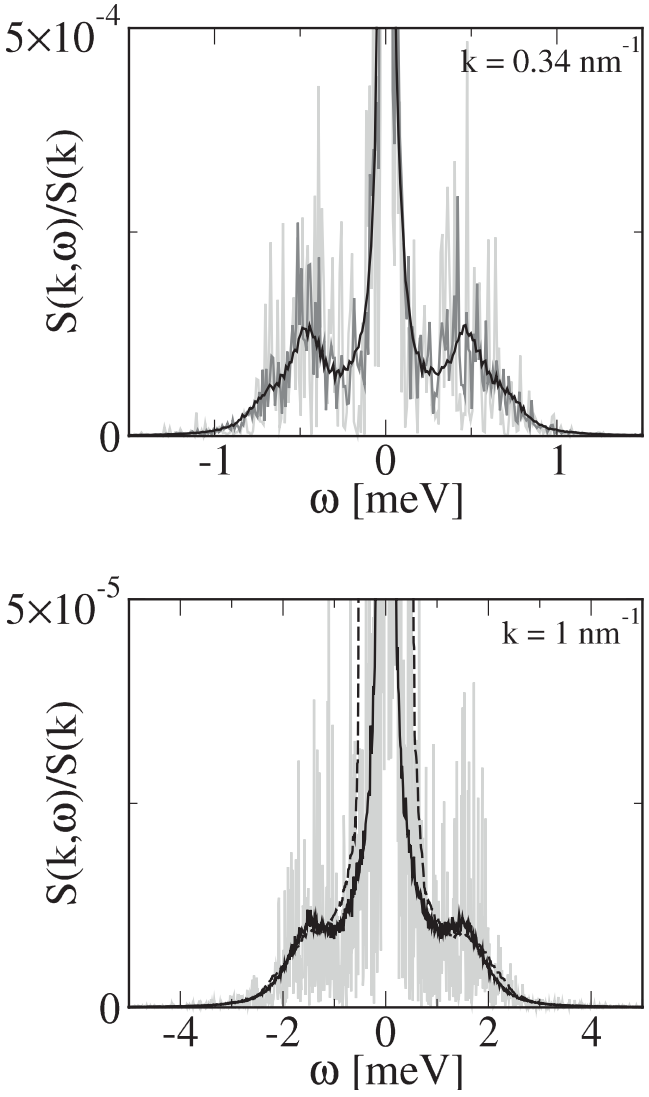

FIGURE 3 The dynamic structure factor may be described as a Rayleigh-Brillouin triplet in the low k domain. (*Top*) Raw simulation data at $k = 0.34$ nm^{-1} after 0.4 ns (*medium shading*), 2.4 ns (*dark shading*), and 144 ns (*black*). (*Bottom*, *solid lines*) Raw simulation data at $k = 1$ nm^{-1} after 0.4 ns (*shaded*) and 144 ns (*black*). (*Dotted line*) Convolution of the shaded line with a window function of width $\sigma = 1$ meV.

(18, 19), the accuracy of the material constants is improved since better energy resolution was used. This study furnishes the best sampling at all k and ω from MD simulations up to now, and extends the range of k-vectors with approximately one order of magnitude.

The Rayleigh line

The central Rayleigh line is extremely narrow, especially for low k-values, and its width is related to transport of energy. Hydrodynamics suggests that this width is proportional to the wave vector squared, with the proportionality constant being the thermal diffusivity, D_T. Correlation function data up to 400 ps in the time domain permits a resolution in energy transfer of 0.01 meV. This was found to be insufficient at low wave vectors, whereas the separation of the Brillouin and Rayleigh lines was problematic at high wave vectors where the precision was sufficient. Therefore, we extended the part of the correlation functions used up to 4 ns, which allowed an energy resolution of 0.001 meV, but with more poor precision at the lowest energies. The width of the Rayleigh peak was determined from a least-squares fit to a Lorentzian shape. By plotting the fitted data versus wave vector, and focusing on intermediate values of k, we were able to establish a quadratic dependence of Γ_h upon k (Fig. 4). The error bars for low k were still large since the width of the Rayleigh line is close to, or below, the energy resolution. Thus, a thermal diffusivity $D_T = (4.2 \pm 0.05) \times 10^{-11}$ m^2 s^{-1} (Table 1) was obtained. We note that this gives a time constant $\tau = \Gamma_h^{-1} = (D_T k^2)^{-1}$ for an exponentially decaying intermediate scattering function that is 200 ns at $k = 0.34$ nm^{-1}, 24 ns at $k = 1$ nm^{-1}, and 200 ps at $k = 30$ nm^{-1}. These numbers show why we have serious resolution problems.

The other way to go if data is too coarse to resolve the Rayleigh line is to use a window function in the fashion presented in Methods. The width of a Lorentzian-shaped window

TABLE 1 Material constants determined from the low k domain of $S(k, \omega)$ from these simulations, inelastic x-ray scattering experiments and earlier MD studies

Parameter	c [m s^{-1}] $\times 10^{-3}$	D_T [m^2 s^{-1}] $\times 10^{10}$	β [m^2 s^{-1}] $\times 10^7$
This article		0.42 ± 0.05	2.8 ± 0.6
$\omega_s = ck$	1.670 ± 0.084		
$\omega_s = ck - c_3k^3$	1.989 ± 0.100		
Chen et al. (18)	1.717	7.6 ± 3.0	~2
Tarek et al. (19)	1.370	6.8 ± 3.5	~3
Fluid Argon (44)	0.870	980	2.1

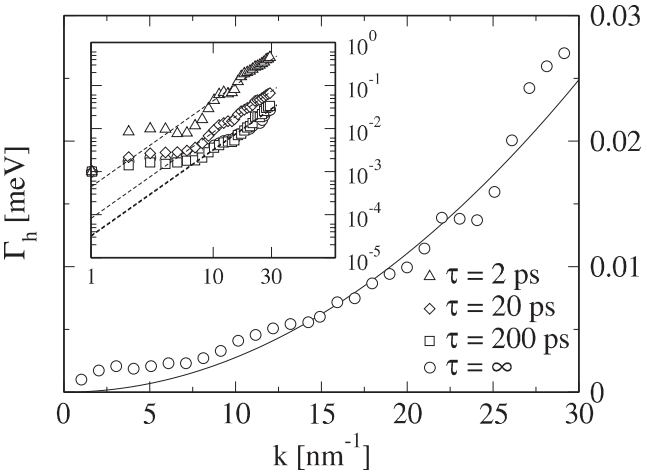

FIGURE 4 The width of the Rayleigh line, Γ_h, calculated by fitting simulation data to Eq. 15 (*circles*). (*Solid line*) Quadratic fit, $\Gamma_h(k) = D_T k^2$, to the circles in the low and intermediate domains ($k < 20$ nm^{-1}) with $D_T = (0.42 \pm 0.05) \times 10^{-10}$ m^2/s. (*Inset*) Logarithmic plot of the Γ_h obtained after convolution of the raw data with window functions that have different exponential falloff times. (*Dashed lines*) Quadratic fits. The width of the window function has been subtracted. The bias on data increases as τ decreases, changing D_T (Table 2).

function can be subtracted in the analysis to obtain the true power spectrum. However, the use of a window function limits the frequency resolution of the spectrum and influences, therefore, the calculated diffusivities. This can be seen in the inset of Fig. 4 where the width of the Rayleigh line from our raw data is compared to the width obtained from the same data after convolution with window functions of different falloff times τ, and subtraction of the corresponding window width, σ. The thermal diffusivity D_T changes with more than one order of magnitude (Table 2).

We also note that it is difficult to obtain a good fit of the Rayleigh line to a single Lorentzian. The top of the peak is too narrow to match the width close to the base. A considerably better fit can be obtained by using two Lorentzians that differ approximately one order-of-magnitude in width (Fig. 5). The two peaks translates to two exponential relaxation processes in the time domain

$$F(k,t) = \alpha e^{-\Gamma_{h1} t} + (1-\alpha) e^{-\Gamma_{h2} t}. \quad (18)$$

Similar dynamics has been reported from neutron scattering experiments on fluid lipid membranes (17,43). In Fig. 6 , the intermediate scattering function, $F(k, t)$, obtained from the simulations is compared to single- and double-exponential fits, for a few selected values of k. The amplitude α determines the dominating process and generally the fast process seem to dominate for large k, and the other way around for low k. Both line-widths in Eq. 18 vary quadratically with k but with different prefactors: 4.0×10^{-11} m^2 s^{-1} and 6.5×10^{-10} m^2 s^{-1}. The proportionality constant for the first (slow) relaxation process is similar to the thermal diffusivity obtained in the previous fit and gives the very narrow central part of the Rayleigh peak. The second (faster) process gives the broader base of the Rayleigh peak and is similar to the thermal diffusivity reported by the literature (1,19). The different prefactors could be interpreted as thermal diffusivities on separate timescales due to different heat conduction mechanisms, but this remains to be worked out in detail.

The position of the Brillouin lines

The Brillouin doublet consists of two phonon modes that correspond to propagating adiabatic waves in the membrane. In $S(k, \omega)$ these lines are characterized by their width, Γ_s, and their position, $\pm\omega_s$ (Fig. 1). We constructed the dispersion relations $\omega_s = \omega_s(k)$ and $\omega_{max} = \omega_{max}(k)$ from data. To be coherent with the common nomenclature of generalized hydrodynamics, $\omega_{max}(k)$ is the angular frequency at the maximum for the longitudinal current correlation function,

TABLE 2 Influences on the thermal diffusivity D_T from the use of a window function with different falloff times τ

τ [ps]	2	20	200	∞
D_T [m^2 s^{-1}] $\times 10^{10}$	7.7	1.3	0.43	0.42

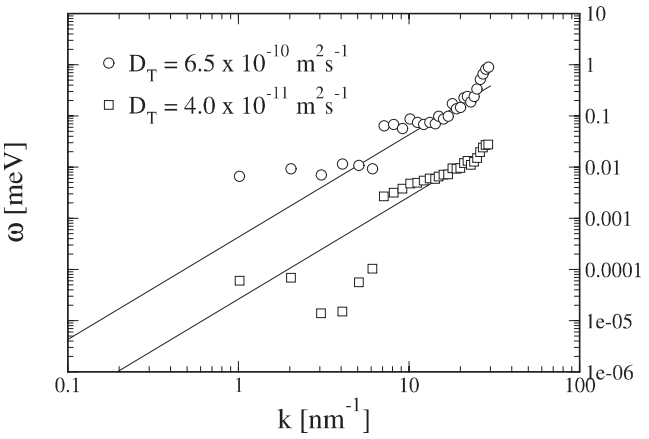

FIGURE 5 The fit of the Rayleigh peak can be improved by assuming two Lorentzian functions instead of one. One is a narrow peak, similar to the fit of a single Lorentzian, and the other peak has a broader line width. The thermal diffusivities obtained from a quadratic fit to the two line-widths are 4.2×10^{-11} m^2 s^{-1} and 6.5×10^{-10} m^2 s^{-1}. For small values of k, the fitted values are uncertain.

$J(k, \omega)$. These two similar, but different, quantities have a tendency to be mixed up and regarded as equal. This is not the case, as ω_s is defined in Eq. 15, and ω_{max} is defined from

$$\frac{\partial}{\partial\omega} J(k,\omega)\bigg|_{\omega=\omega_{max}} = 0. \quad (19)$$

Since $J(k, \omega) = (\omega^2/k^2)S(k, \omega)$, it follows that $\omega_s \neq \omega_{max}$. That said, there are obvious similarities between their dispersion relations (Fig. 7).

The quantity $\omega_{max}(k)$ shows a behavior that has also been observed in simple liquids (see, e.g., (6)). The phonon dispersion is linear for small k and reaches a maximum at ~7 nm^{-1} before decreasing to a nonzero minimum at $\sim k_G = 14.3$ nm^{-1}. The wave vector k_G represents the position of the chain-chain correlation peak in the static structure

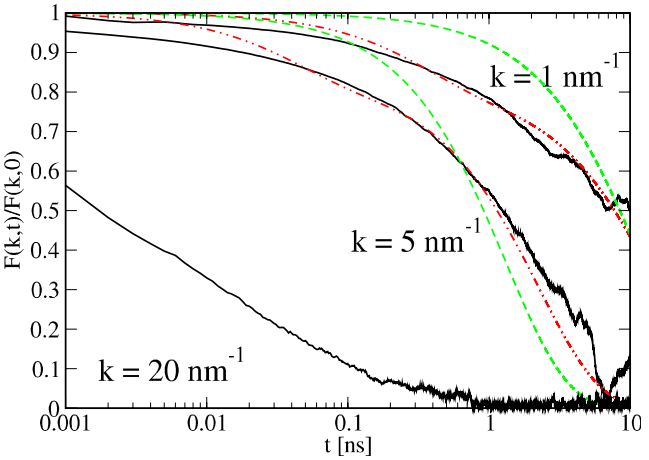

FIGURE 6 The intermediate scattering function $F(k, t)$ at 1, 5, and 20 nm^{-1}. (*Solid lines*) Calculated from the simulation data. (*Dashed lines*) Fits to single exponentials. (*Dashed dotted lines*) Fits to the sum of two exponentials (Eq. 18).

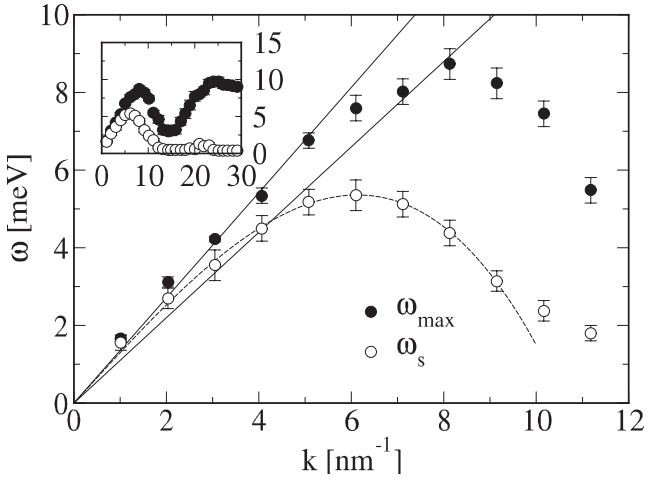

FIGURE 7 Position of the Brillouin lines, ω_s, and the position of the maximum of the current correlation function, ω_{max}, calculated from a fit of simulation data to Eq. 15 (*circles*). (*Solid lines*) Linear fits to the solid and open circles at $k < 5$ nm^{-1}, and (*dotted line*) fit to $\omega_s(k)$ with a first correction term included. (*Inset*) $\omega_s(k)$ and $\omega_{max}(k)$ in all domains of the spectrum. A dispersion gap is visible at $\sim k_G = 14.3$ nm^{-1}.

factor (Fig. 8) and relates to a characteristic distance $2\pi/k_G \approx 0.44$ nm between the hydrocarbon tail groups. After that the curve increases more or less linearly again.

The quantity $\omega_s(k)$ shows similar features but also important differences. The dispersion curve maximum is lower than for $\omega_{max}(k)$ and located at 6 nm^{-1}. In hydrodynamic theory, $\omega_s(k) = ck + O(k^3)$; i.e., a linear function with a first higher-order cubic correction term. Fig. 7 shows that although the linear approximation for $\omega_s(k)$ is quite good for small k, the inclusion of the next term furnishes a description that is valid also for intermediate k-values. Without the cubic term, the sound velocity becomes $c = 1670 \pm 84$ m s^{-1}. With the cubic term, the larger value $c = 1989 \pm 100$ m s^{-1} is obtained.

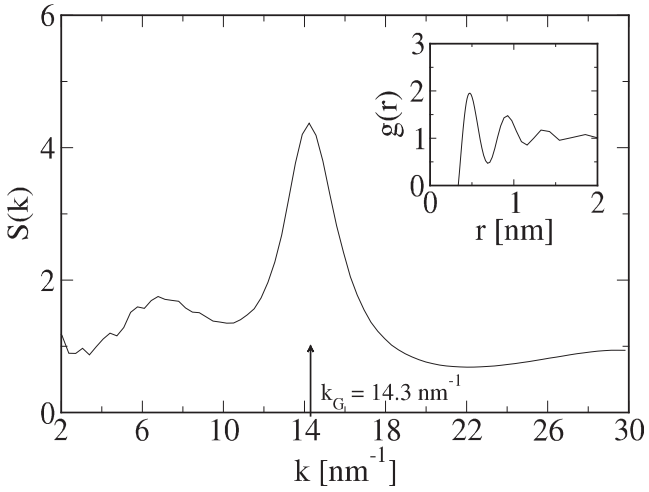

FIGURE 8 The calculated static structure factor, $S(k)$, from our simulations. $k_G = 14.3$ nm^{-1} is a well-known peak, characteristic of the hydrocarbon chain-chain distance. (*Inset*) Pair distribution function $g(r)$ obtained by Fourier transformation of $S(k)$.

The width of the Brillouin lines

The Brillouin lines are several orders-of-magnitude broader than the Rayleigh line and it is therefore a relatively simple task to resolve them from MD simulation data. They arise from pressure fluctuations in the system (6) which propagate with the sound velocity c, on lifetimes $\sim\Gamma_s^{-1}$. Wider Brillouin lines means that these phonons decay faster.

As shown in the Theory section, the predicted width of the Brillouin lines is $\Gamma_s(k) = \beta k^2$, where β is the sound attenuation coefficient. The value β determines the damping of the sound modes in the system, in a similar manner to D_T, in the case of the Rayleigh mode. In contrast to the Rayleigh line, the Brillouin lines show a linear growth of the width for small k. This suggests another behavior in the hydrodynamic limit than predicted from theory. Still, a fit of data to a quadratic function could be performed in the low k domain, although deviations are evident (Fig. 9). We note that the value of the sound attenuation coefficient obtained from this procedure, $\beta = (2.8 \pm 0.6) \times 10^{-7}$ m^2 s^{-1}, is similar to values calculated from MD data on liquid Argon (44). Further, when extending the analysis of $\Gamma_s(k)$ over all domains of the spectrum, one finds resemblance between $\omega_{max}(k)$ and $\Gamma_s(k)$ (Figs. 7 and 9, *insets*). This implies a connection between the lifetime of the pressure fluctuations represented by the phonon modes and the current fluctuations in the system.

The asymmetric contribution to the Brillouin lines is

$$\xi(k) = [\beta + D_T(\gamma - 1)]c^{-1} \equiv \zeta k, \qquad (20)$$

so that $\zeta \approx \beta/c$ if $\beta >> D_T$. By determining ζ from the power spectrum and using our calculated value of c, we obtain $\beta \approx 5.1 \times 10^{-7}$ m^2 s^{-1}—which is larger than the value obtained from a fit of the line-width to a quadratic function.

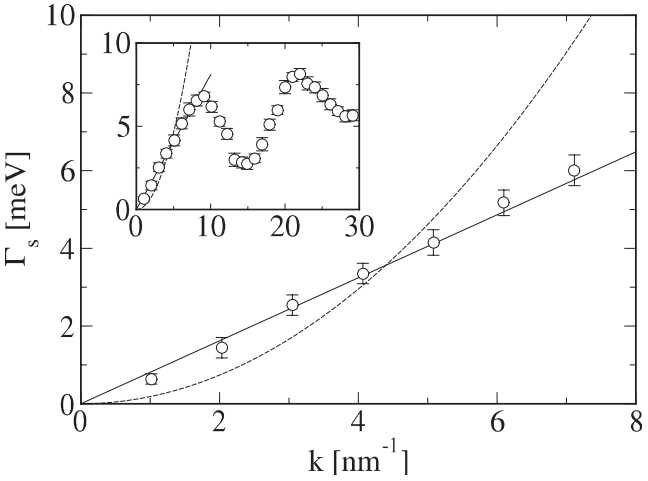

FIGURE 9 The width of the Brillouin lines, Γ_s, in the hydrodynamic limit calculated from a fit of simulation data to Eq. 15 (*circles*). Data shows a linear relation (*solid line*) up to $k = 8$ nm^{-1}, not a quadratic (*dotted line*) as predicted by hydrodynamic theory. A best fit to a quadratic dependence yields a sound attenuation coefficient $\beta = (2.8 \pm 0.6) \times 10^{-7}$ m^2 s^{-1}. (*Inset*) $\Gamma_s(k)$ in all domains of the spectrum.

The asymmetry, as reflected by $\xi(k)$, is more pronounced for larger values of k. In light scattering experiments, where k typically is ~0.01 nm^{-1}, the asymmetry is difficult to detect because ζ is ~0.1 nm, resulting in Brillouin lines that are almost perfect Lorentzians. For larger wave vectors of ~0.1–10 nm^{-1}, probed in, e.g., MD simulations and x-ray or neutron scattering experiments, the asymmetry may be more important. From our results, one sees that $\xi(k)$ is ~0.05 at $k = 0.34$ nm^{-1}, which results in quite symmetric Brillouin lines; the lines are quite asymmetric at $k = 5$ nm^{-1}, where $\xi(k)$ is of order unity.

The Landau-Placzek ratio

The Lorentzian line shapes in Eq. 15 lead to some simple results for the integrated intensities of the Rayleigh mode, I_R, and each of the Brillouin modes, I_B (note that the asymmetric parts of the Brillouin modes do not contribute to the integrated intensity):

$$I_R = \frac{\gamma - 1}{\gamma} S(k) \text{ and} \qquad (21)$$

$$I_B = \frac{1}{2\gamma} S(k).$$

From this the Landau-Placzek ratio (45) is defined as $R_{LP} \equiv I_R/2I_B$, which gives $R_{LP} = \gamma - 1$ (with $\gamma = c_P/c_V$). In the k range studied (0.34–30 nm^{-1}), the modes overlap to varying extent, so a reasonable numerical value would hint that the separation of the modes has been properly done. In principle, this also provides a way to determine c_P/c_V from the simulations, but in practice it turns out that the uncertainty is too large for this to be of much value.

There are difficulties with a direct numerical integration of the three peaks. The lines overlap increasingly with growing k, making it impossible to separate the thermal and acoustic contributions unless k is fairly small (<5 nm^{-1}). On the other hand, the width of the central Rayleigh line, Γ_h, is approximately three-orders-of-magnitude smaller than that of the Brillouin lines, Γ_s. The Rayleigh line will thus be a single point at $\omega = 0$, unless one would go to large k, which would make the peak separation problematic. We chose to sacrifice a rigorous test of the shape of the Rayleigh peak and assume that it is

$$S_R(k, \omega) = \frac{S_{max}}{1 + (\omega/\Gamma_h)^2}, \qquad (22)$$

which has the Lorentzian properties $S_R(k, \Gamma_h) = S_{max}/2$ and $S_R(k, 0) = S_{max}$ as expected. Then $I_R = \pi\Gamma_h S_{max}$, where S_{max} is accurately determined from the point at $\omega = 0$ and Γ_h from fitting a few points close to $\omega = 0$ to a Lorentzian function. The value I_B could then be determined by numerical integration of $S(k, \omega)$ as $I_B = I_{tot} - I_R$ (Eqs. 14 and 21). This resulted in the Landau-Placzek ratios shown versus k in Fig. 10 . We obtain the value of the specific heat ratio $\gamma = 1.06 \pm 0.01$. We are not aware of any direct measurements of this ratio for lipid bilayers, but the specific heat ratio may be written as

$$\gamma = \left(1 - \frac{\alpha^2 T}{n\kappa c_P}\right)^{-1}, \qquad (23)$$

using exact thermodynamic relations. Here, α is the thermal expansion coefficient, κ the isothermal compressibility, n is the number density, and T the absolute temperature. The material constants are experimentally known, but with low precision (both the isothermal compressibility and the thermal expansion coefficient suffers from uncertainties of ~50%). Based on literature data (see, e.g., the compilation in (42)), one obtains $\gamma = 1.04$–1.20, depending on the specific values used for κ and α. For what it is worth, we note that γ calculated from the Landau-Placzek ratio of the simulations falls in this interval.

DISCUSSION

Considerable effort has been put into understanding liquids in terms of generalized hydrodynamics. Studies have been conducted using a variety of methods including inelastic x-ray scattering (1), inelastic neutron scattering (2,4,43), neutron spin-echo techniques (17), and computer simulations (3,19) to determine the space and time Fourier-transform of the density-density correlation function, the elusive $S(k, \omega)$. Attention was initially directed toward simple systems such as Lennard-Jones fluids, and in recent time more complex systems, such as lipid bilayers, have gained interest. In the later category, this work is, to the best knowledge of the authors, the computational study that thus far covers to the most extensive (k, ω) regime. The dynamics of complex fluids, of which lipid bilayers are one example,

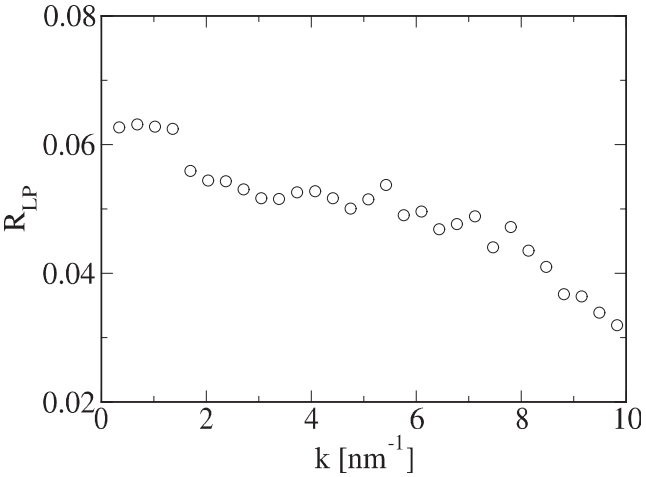

FIGURE 10 Landau-Placzek ratio calculated by numerical integration (*circles*) as described in the text. The calculations are not well founded for $k > 5$ nm^{-1} because a separation of the modes is unworkable. In the low k domain, we find $R_{LP} = 0.06 \pm 0.01$, corresponding to a specific heat ratio $\gamma = 1.06 \pm 0.01$.

is generally complicated. In many processes of such kind, parts of the correlation functions decay very slowly and the systems undergo large fluctuations. This type of dynamics can have biological significance; fluctuations in lipid membranes are important since they may affect the permeability of the membrane for different molecules, thus changing the properties of biological transport processes. However, a biological membrane is much more complex than a model bilayer like that of this study, and contains different types of lipids, proteins as well as ions. This work could therefore be seen as one of the first steps toward a more coherent understanding of this type of phenomena.

Due to a large system (1024 lipids), wave vectors down to $k = 0.34\ \mathrm{nm}^{-1}$ can be analyzed. The length of the simulations permits an energy resolution of 0.01 meV without too much noise. The statistical quality of the data has been improved by sampling several independent simulations and has allowed for a rigorous investigation of the dynamics in lipid bilayers in terms of a three-mode dynamic structure factor. We have made an effort to probe the behavior of the membrane in the hydrodynamic limit. The study confirms that a three-mode function is useful for $S(k, \omega)$ in the low and intermediate domains, up to $\sim 20\ \mathrm{nm}^{-1}$, after which a high k regime enters where the Rayleigh mode dominates the spectrum. However, the behavior predicted by standard hydrodynamic theory is only valid in the low domain, until $\sim 5\ \mathrm{nm}^{-1}$, whereupon the Rayleigh-Brillouin triplet tends to overlap so much that the three lines cannot be separated.

The width of the Rayleigh line is so narrow that a resolution of $\Delta\omega = 0.01$ meV was inconclusive for a full mapping. The relation $\Gamma_h(k) = D_T k^2$, predicted by theory, could be tested and was found to hold. The value of D_T found by fitting the Rayleigh peak data to one single Lorentzian is approximately one-order-of-magnitude smaller than earlier reported results (1,19). However, a much better fit is obtained using two Lorentzian functions. One of the line-widths is then very similar to that of the single Lorentzian fit and corresponds to an exponential relaxation process with a time constant of 200 ns for the lowest wave vector ($0.34\ \mathrm{nm}^{-1}$) accessible in this study, and <100 ps at the other end of the wave vector interval. The second peak is broader and represents a relaxation process that is approximately one-order-of-magnitude slower. The thermal diffusivity obtained from the width of this peak is similar to those reported in previous studies (1,19). The same type of dynamics with two different relaxation processes on separate timescales has been reported by the literature (17,43) in studies using inelastic neutron scattering on stacked DMPC bilayers. Our simulations agree with their results, even though our data is limited in its statistical accuracy for long times and low wave vectors. Scattering experiments on DPPC lipids at higher temperatures (46) have also shown that the shape and the decay of the intermediate scattering function can be complex. Longer, large-scale MD simulations are needed to explore the details of these correlation functions.

Further, we explicitly show that the use of a window function, which broadens the spectrum lines, heavily influences D_T (Table 2).

The positions of the Brillouin lines followed a linear relation, $\pm\omega_s(k) = \pm ck$, in the low k domain as expected in the hydrodynamic limit. The extracted sound velocity c was very similar to earlier studies (18). If a first-order, cubic correction from hydrodynamic theory was included in the description so that $\omega_s(k) = ck - c_3k^3$, the prediction was accurate in the intermediate domain as well. This gives a slightly larger value for c. Here, c_3 is a function of material constants appearing in Eq. 11. A comparison of its value, obtained from a fit to that which can be calculated from the specific material constants, is of little use, because the experimental values of these constants are too uncertain.

A dispersion gap, when the Brillouin doublet centers at $\omega = 0$ was found to emerge at $\sim k_G$, the chain-chain correlation peak of the static structure factor. This corresponds to a situation where mechanic waves that spread in the membrane on large length scales are damped at short length scales until propagation ceases. Similar dispersion gaps have been found in simple liquids (47) and have also been suggested to occur in lipid bilayers (3). Our results support these suggestions.

The width of the Brillouin lines was more than two-orders-of-magnitude larger than that of the Rayleigh line and could be determined accurately down to low k. For k-values up to $8\ \mathrm{nm}^{-1}$, a linear relation between the line width and the wave vector was found instead of the quadratic one predicted by theory, and presumed in earlier studies with coarser k-resolution. We do not have a theoretical explanation for this, but as seen from the error bars in Fig. 9 this is not due to statistical errors. The widths of the Rayleigh lines seem to be in quantitative agreement to the results obtained from MD simulations (3,19) and x-ray scattering experiments (1).

The Landau-Placzek ratio R_{LP} was calculated for small k, when the lines of $S(k, \omega)$ was most separated as a Rayleigh-Brillouin triplet. It turned out to be nontrivial to account for the overlap of the peaks in all domains of the spectrum. The best results were obtained for the lowest k-values where R_{LP} converged to 0.06 ± 0.01, which compares to a rough estimate from thermodynamic relations in the interval 0.04–0.20. From this, we may only conclude that our result is not unreasonable, but both simulation data and experimentally determined material constants for the lipids are too uncertain to give a more conclusive answer.

The size of the system ($\sim 10^5$ atoms) and simulation time (~150 ns of statistics) of this work is touching the upper limit for atomistic simulations at present. Further theoretical studies give promising prospects to reveal the atomistic details and physical natures of the different relaxation processes that contribute to the Rayleigh line. The main lesson to take home is that even though some deviations from hydrodynamic behavior are evident, general hydrodynamic theory is fairly valid up to $\sim 5\ \mathrm{nm}^{-1}$ and $S(k, \omega)$ can be described by three modes up to $\sim 20\ \mathrm{nm}^{-1}$.

O.E. acknowledges support from the Swedish Research Council (Vetenskapsrådet).

REFERENCES

1. Weiss, T. M., P. -J. Chen, H. Sinn, E. E. Alp, S. -H. Chen, et al. 2003. Collective chain dynamics in lipid bilayers by inelastic x-ray scattering. *Biophys. J.* 84:3767–3776.
2. Rheinstädter, M. C., C. Ollinger, G. Fragneto, F. Demmel, and T. Salditt. 2004. Collective dynamics of lipid membranes studied by inelastic neutron scattering. *Phys. Rev. Lett.* 93:108107.
3. Hub, J. S., T. Salditt, M. C. Rheinstädter, and B. L. de Groot. 2007. Short-range order and collective dynamics of DMPC bilayers: a comparison between molecular dynamics simulations, x-ray, and neutron scattering experiments. *Biophys. J.* 93:3156–3168.
4. Rheinstädter, M. C., T. Seydel, W. Häussler, and T. Salditt. 2006. Exploring the collective dynamics of lipid membranes with inelastic neutron scattering. *J. Vac. Sci. Technol. A.* 24:1191–1196.
5. Fleury, P. A., and J. P. Boon. 1969. Brillouin scattering in simple liquids: argon and neon. *Phys. Rev.* 186:244–254.
6. Boon, J. P., and S. Yip. 1980. Molecular Hydrodynamics. McGraw-Hill, New York.
7. Hansen, J. P., and I. R. McDonald. 1986. Theory of Simple Liquids, 2nd Ed. Academic Press, London.
8. Verlet, L. 1967. Computer ''experiments'' on classical fluids. I. Thermodynamical properties of Lennard-Jones Molecules. *Phys. Rev.* 159:98–103.
9. Verlet, L. 1968. Computer ''experiments'' on classical fluids. II. Equilibrium correlation functions. *Phys. Rev.* 165:201–214.
10. Levesque, D., and L. Verlet. 1970. Computer ''experiments'' on classical fluids. III. Time-dependent self-correlation functions. *Phys. Rev. A.* 2:2514–2528.
11. Levesque, D., L. Verlet, and J. Kürkijarvi. 1973. Computer ''experiments'' on classical fluids. IV. Transport properties and time-correlation functions of the Lennard-Jones liquid near its triple point. *Phys. Rev. A.* 7:1690–1700.
12. Rahman, A. 1974. Propagation of density fluctuations in liquid rubidium: a molecular-dynamics study. *Phys. Rev. Lett.* 32:52–54.
13. Rahman, A. 1974. Density fluctuations in liquid rubidium. II. Molecular-dynamics calculations. *Phys. Rev. A.* 9:1667–1671.
14. de Schepper, I. M., P. Verkerk, A. A. van Well, and L. A. de Graaf. 1983. Short-wavelength sound modes in liquid argon. *Phys. Rev. Lett.* 50:974–977.
15. van Well, A. A., P. Verkerk, L. A. de Graaf, J. -B. Suck, and J. R. D. Copley. 1985. Density fluctuations in liquid Argon: coherent dynamic structure factor along the 120-K isotherm obtained by neutron scattering. *Phys. Rev. A.* 31:3391–3414.
16. Edholm, O. 2008. Time and length scales in lipid bilayer simulations. *In* Current Topics in Membranes., Chapt. 3 S. Feller, editor. Elsevier, Dordrecht, The Netherlands.
17. Rheinstädter, M. C., W. Häussler, and T. Salditt. 2006. Dispersion relation of lipid membrane shape fluctuations by neutron spin-echo spectrometry. *Phys. Rev. Lett.* 97:048103.
18. Chen, P. -J., Y. Liu, T. M. Weiss, H. W. Huang, H. Sinn, et al. 2003. Studies of short-wavelength collective molecular motions in lipid bilayers using high resolution inelastic x-ray scattering. *Biophys. Chem.* 105:721–741.
19. Tarek, M., D. J. Tobias, S.-H. Chen, and M. L. Klein. 2001. Short wavelength collective dynamics in phospholipid bilayers: a molecular dynamics study. *Phys. Rev. Lett.* 87:238101.
20. Van Hove, L. 1954. Correlations in space and time and born approximation scattering in systems of interacting particles. *Phys. Rev.* 95:249–262.
21. Mountain, R. D. 1966. Spectral distribution of scattered light in a simple fluid. *Rev. Mod. Phys.* 38:205–214.
22. Boon, J. P., and P. Deguent. 1970. Transport functions and light scattering in simple dense fluids. *Phys. Rev. A.* 2:2542–2550.
23. Van Der Spoel, D., E. Lindahl, B. Hess, G. Groenhof, A. E. Mark, et al. 2005. GROMACS: fast, flexible, and free. *J. Comput. Chem.* 26:1701–1718.
24. Berger, O., O. Edholm, and F. Jähnig. 1997. Molecular dynamics simulations of a fluid bilayer of dipalmitoylphosphatidylcholine at full hydration, constant pressure, and constant temperature. *Biophys. J.* 72:2002–2013.
25. Darden, T., D. York, and L. Pedersen. 1993. Particle mesh Ewald: an *N*log(*N*) method for Ewald sums in large systems. *J. Chem. Phys.* 98:10089–10092.
26. Essmann, U., L. Perera, M. L. Berkowitz, T. Darden, H. Lee, et al. 1995. A smooth particle mesh Ewald method. *J. Chem. Phys.* 103:8577–8593.
27. Berendsen, H. J. C., J. P. M. Postma, W. F. van Gunsteren, A. DiNola, and J. R. Haak. 1984. Molecular dynamics with coupling to an external bath. *J. Chem. Phys.* 81:3684–3690.
28. Nosé, S. 1984. A molecular dynamics method for simulations in the canonical ensemble. *Mol. Phys.* 52:255–268.
29. Hoover, W. G. 1985. Canonical dynamics: equilibrium phase-space distributions. *Phys. Rev. A.* 31:1695–1697.
30. Parrinello, M., and A. Rahman. 1981. Polymorphic transitions in single crystals: a new molecular dynamics method. *J. Appl. Phys.* 52:7182–7190.
31. Nosé, S., and M. L. Klein. 1983. Constant pressure molecular dynamics for molecular systems. *Mol. Phys.* 50:1055–1076.
32. Kucerka, N., Y. Liu, N. Chu, H. I. Petrache, S. Tristram-Nagle, et al. 2005. Structure of fully hydrated fluid phase DMPC and DLPC lipid bilayers using x-ray scattering from oriented multilamellar arrays and from unilamellar vesicles. *Biophys. J.* 88:2626–2637.
33. Nagle, J. F., and S. Tristram-Nagle. 2000. Structure of lipid bilayers. *Biochim. Biophys. Acta. Biomembr.* 1469:159–195.
34. Smith, G. S., E. B. Sirota, C. R. Safinya, R. J. Plano, and N. A. Clark. 1990. X-ray structural studies of freely suspended ordered hydrated DMPC multimembrane films. *J. Chem. Phys.* 92:4519–4529.
35. Frigo, M., and S. Johnson. 2005. The design and implementation of FFTW3. *Proc. IEEE.* 93:216–231.
36. Levenberg, K. 1944. A method for the solution of certain non-linear problems in least square. *Q. Appl. Math.* 2:164–168.
37. Marquardt, D. 1963. An algorithm for least-squares estimation of nonlinear parameters. *SIAM J. Appl. Math.* 11:431–441.
38. De Gennes, P. G. 1959. Liquid dynamics and inelastic scattering of neutrons. *Physica.* 25:825–839.
39. Tabony, J., and B. Perly. 1991. Quasielastic neutron scattering measurements of fast local translational diffusion of lipid molecules in phospholipid bilayers. *Biochim. Biophys. Acta. Biomembr.* 1063:67–72.
40. LePesant, J. -P., L. Powers, and P. S. Pershan. 1978. Brillouin light scattering measurement of the elastic properties of aligned multilamellar lipid samples. *Proc. Natl. Acad. Sci. USA.* 75:1792–1795.
41. Manglkammer, W., and J. Krüger. 2005. Brillouin scattering of lipid membranes. *J. Phys. IV (Fr).* 129:65–67.
42. Heimburg, T. 1998. Mechanical aspects of membrane thermodynamics. Estimation of the mechanical properties of lipid membranes close to the chain melting transition from calorimetry. *Biochim. Biophys. Acta.* 1415:147–162.
43. Rheinstädter, M. C., T. Seydel, and T. Salditt. 2007. Nanosecond molecular relaxations in lipid bilayers studied by high energy-resolution neutron scattering and in situ diffraction. *Phys. Rev. E Stat. Nonlin. Soft Matter Phys.* 75:011907.
44. Schoen, M., R. Vogelsang, and C. Hoheisel. 1986. Computation and analysis of the dynamic structure factor $S(k, \omega)$ for small wave vectors. *Mol. Phys.* 57:445–471.
45. Landau, L., and G. Placzek. 1934. The structure of undisplaced scattered lines. *Physik Z. Sowjetunion.* 5:172.
46. Doxastakis, M., V. G. Sakai, S. Ohtake, J. K. Maranas, and J. J. de Pablo. 2007. A molecular view of melting in anhydrous phospholipidic membranes. *Biophys. J.* 92:147–161.
47. de Schepper, I. M., and E. G. D. Cohen. 1982. Very-short-wavelength collective modes in fluids. *J. Stat. Phys.* 27:223–281.